CHAPTER 4

MECHANICAL AND ELECTROCHEMICAL

BEHAVIOR OF $\text{Fe}_{(100-x)}\text{Ni}_{(x)}$ ALLOYS

The present chapter describes the synthesis of $\text{Fe}_{(100-x)}\text{Ni}_{(x)}$ alloy specimens with x= 10, 20, 30, 40, and 50 (wt.%) named $\text{Fe}_{90}\text{Ni}_{10}$, $\text{Fe}_{80}\text{Ni}_{20}$, $\text{Fe}_{70}\text{Ni}_{30}$, $\text{Fe}_{60}\text{Ni}_{40}$ and $\text{Fe}_{50}\text{Ni}_{50}$ via powder metallurgy route. Sintering was done at three different temperatures i.e. 1000°C/1h, 1200°C/1h and 1250°C/1h. The detailed synthesis process is already described in previous chapter(Section 3.1). Brief of synthesis can be understood from synthesis flow diagram as shown in Fig. 4.1.
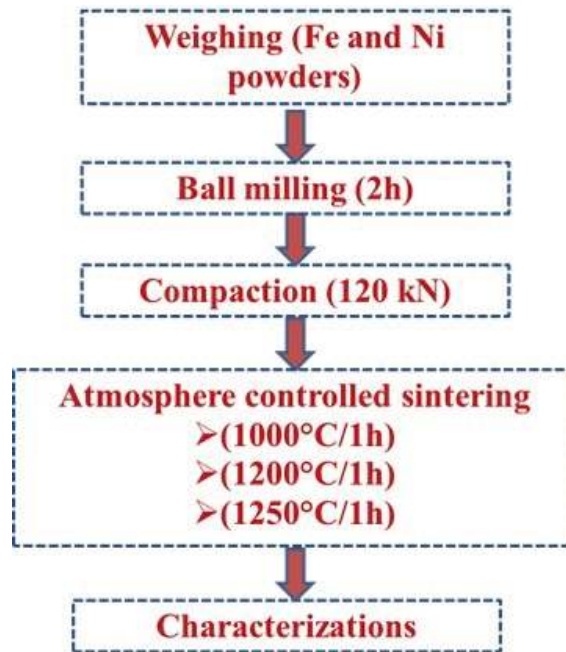

FIGURE 4.1: Synthesis flow diagram of $\text{Fe}_{(100-x)}\text{Ni}_{(x)}$ alloy specimens via powder metallurgy.

This chapter also elaborates the physical, mechanical and electrochemical behavior

of synthesized alloys. Physical properties included phase, microstructure, and density, whereas in mechanical testing, hardness and dry sliding wear properties are examined. In the electrochemical characterization, corrosion test of 1250°C/1h sintered thin polished specimens was performed in simulated sea water solution (3.5 wt.% NaCl aqueous solution). SEM examination of specimen surfaces is done on worn and corroded surfaces after the test to compare with the surfaces of as-prepared specimens.

4.1 X-ray Diffraction (XRD)

4.1.1 X-ray diffraction of raw and ball milled powders

Fig. 4.2 shows X-ray diffraction patterns of (a) Fe raw powder, (b) Ni raw powder and (c) $Fe_{70}Ni_{30}$ ball milled powders.

Obtained patterns were matched with the standard reference files. Fe pattern is matched with JCPDS 06-0696 and Ni pattern is matched with JCPDS 04-0850. As there are no oxide peaks observed in the raw powders, therefore, the above powders are chosen to be used for the synthesis of alloy specimens. Ball milled powders do not show any XRD peak of alloy phase, which confirm the absence of mechanical alloying during ball milling.

4.1.2 X-ray diffraction of sintered specimens

Fig. 4.3 shows X-ray diffraction patterns of $Fe_{(100-x)}Ni_{(x)}$ specimens sintered at 1000°C. Presence of α-Fe (JCPDS: 06-0696), α-(Fe,Ni) (JCPDS: 37-0474) and γ-(Fe,Ni) (JCPDS:
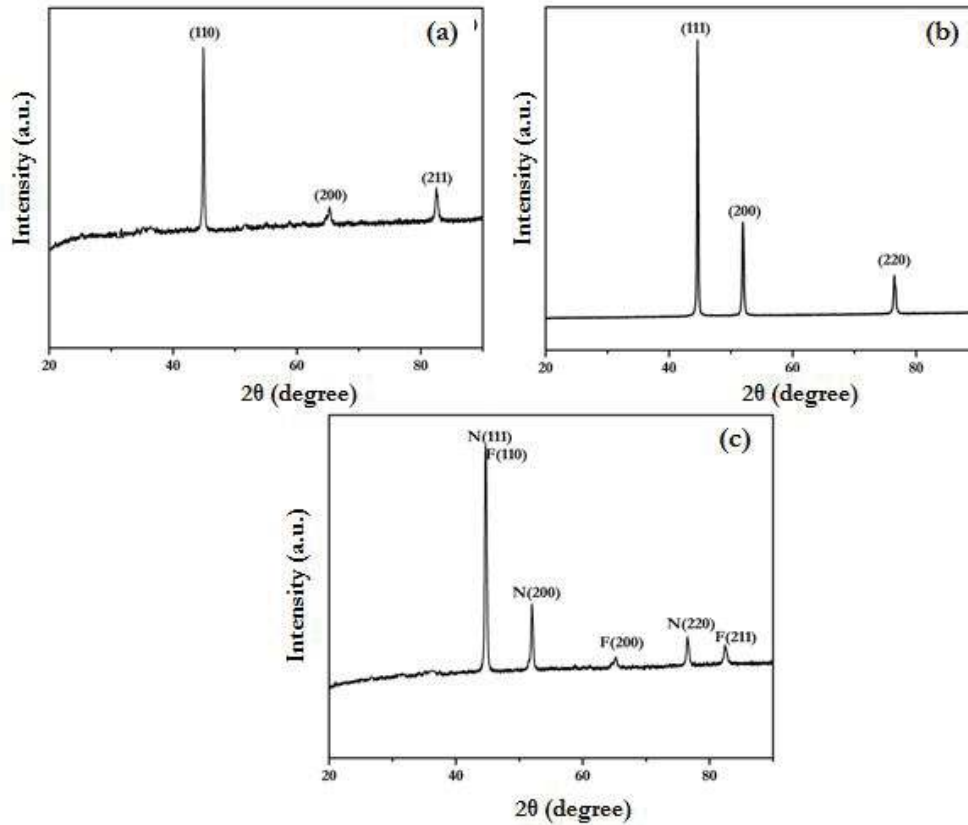
FIGURE 4.2: XRD patterns of (a) Fe, (b) Ni and (c) ball milled ($Fe_{70}Ni_{30}$) powder.

47-1405) is observed in the specimens after sintering. At 1000°C, $Fe_{90}Ni_{10}$ specimen is found to contain α-Fe /α-(Fe,Ni) as major phase and γ-(Fe,Ni) as a minor phase. Since the concentration of Ni is only 10 wt.% and sintering temperature is low, less γ-(Fe,Ni) has formed due to lower inter-diffusion between Fe and Ni elements. As the Ni content is increased from 10 to 50 wt.% , more diffusion of Ni resulted in increased γ-(Fe,Ni) peak intensities while the peak intensities of /α-(Fe,Ni) phase decreased.

Fig. 4.4 shows X-ray diffraction patterns of specimens sintered at 1200°C. α-Fe (JCPDS: 06-0696); α-(Fe,Ni) (JCPDS: 37-0474) and γ -(Fe,Ni) (JCPDS: 47-1405) are observed in the XRD patterns of specimens after sintering at this temperature. Again at
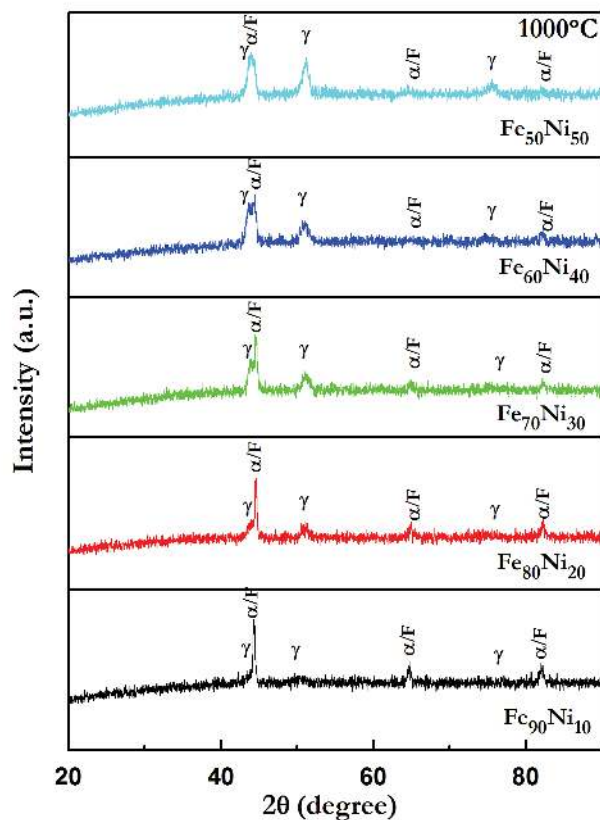
FIGURE 4.3: X-ray diffraction patterns of specimens sintered at 1000°C.

lower Ni concentration, XRD pattern shows major α-Fe/ α-(Fe,Ni) peaks with small γ-(Fe,Ni) peaks. Increasing the Ni concentration from 10 to 50 wt.% resulted in enhanced inter diffusion of Fe and Ni. Therefore, peak intensities of γ-(Fe,Ni) increased, while the peak intensities of α-Fe/ α-(Fe,Ni) decreased with increasing Ni content.

Fig. 4.5 shows X-ray diffraction patterns of $Fe_{(100-x)}Ni_{(x)}$ specimens sintered at 1250°C. α-Fe (JCPDS: 06-0696), α-(Fe,Ni) (JCPDS: 37-0474) and γ-(Fe,Ni) (JCPDS: 47-1405) are observed in the specimens after sintering. Specimens with less Ni concentrations have shown the presence of more intense α-Fe/α-(Fe,Ni) peaks and less intensity
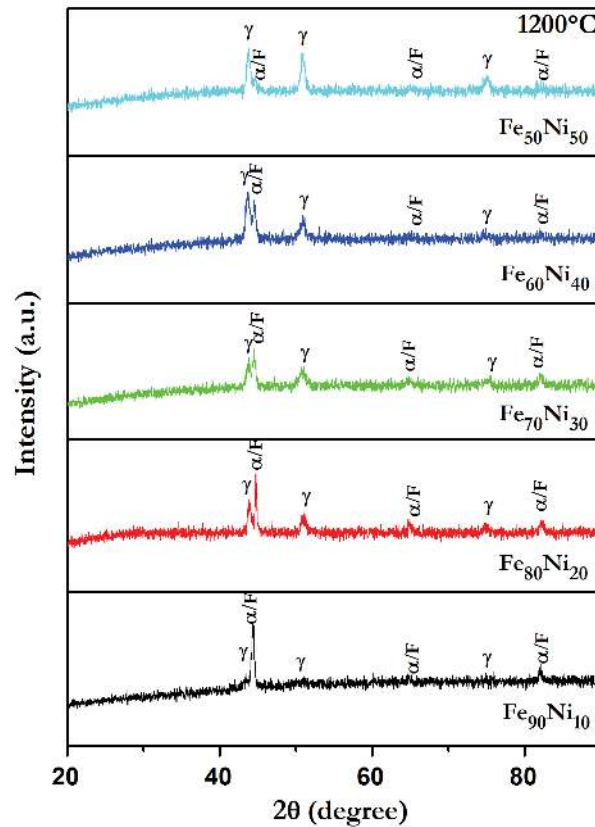
FIGURE 4.4: X-ray diffraction patterns of specimens sintered at 1200°C.

γ-(Fe,Ni) peaks. Increasing the Ni concentration from 10 to 50% resulted in increased γ-(Fe,Ni) peak intensities. Maximum intensity α-(Fe,Ni) peaks are observed in $Fe_{90}Ni_{10}$ and maximum intensity γ-(Fe,Ni) peaks are observed in $Fe_{50}Ni_{50}$.

By comparing Fig. 4.3, Fig. 4.4, Fig. 4.5, it is concluded that increasing the Ni concentration results in more γ-(Fe,Ni) phase formation. It is also observed that the change in γ-(Fe,Ni) peak intensities also result with the change in sintering temperature. When the sintering temperature is increased from 1000-1200°C, an increase in the γ-(Fe,Ni) peak intensities is observed for the same compositions.
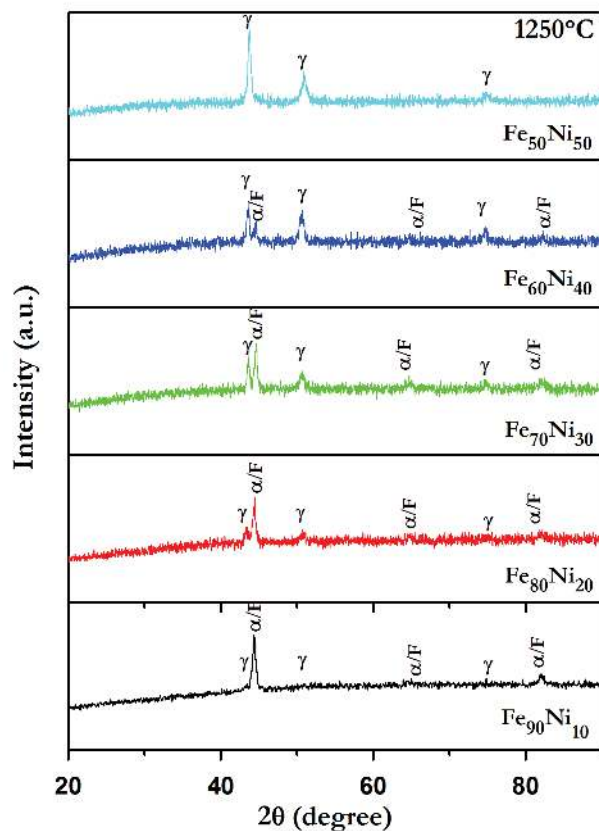
FIGURE 4.5: X-ray diffraction patterns of specimens sintered at 1250°C.

At 1250°C, the increase in γ-(Fe,Ni) peak intensities for all the compositions are observed as compared to 1000 and 1200°C sintered specimens. From the Fe-Ni phase diagram [109], single BCC-α alloy phase formation occurs up to 6% Ni nickel concentration below 900°C during cooling. A combined BCC-α + FCC-γ phase formation in a broad region results at higher Ni content. The previous studies [110] showed a duplex microstructure, containing both α and γ phases for Fe-Ni powder mixtures even after sintering up to 1350°C due to compositional inhomogeneity. In the present study, it is observed from phase analysis that formation of γ-(Fe,Ni) increased at higher temperatures

66

(Fig. 4.3 to Fig. 4.5). Initially, both α-(Fe,Ni) and γ-(Fe,Ni) phases precipitate from solid interface between Fe and Ni at 1000°C. This results in the enhancement of γ-(Fe,Ni) with increasing sintering temperature. It is interesting to note that for $Fe_{50}Ni_{50}$, maximum γ-(Fe,Ni) formation occurs at 1250°C instead of a duplex phase. No significant peak of any other phase is observed at this temperature from XRD. This supports the high diffusion rate of elements at higher sintering temperatures.

As both α-Fe and α-(Fe,Ni) have similar crystalline structures and their character-istic diffraction patterns are very close, therefore, it is difficult to distinguish them. The combined effect of Ni concentration and sintering temperature is found responsible for the enhanced diffusion between Fe and Ni elements. Therefore the maximum peak inten-sity is observed in specimen $Fe_{50}Ni_{50}$ after sintering at 1250°C with minimum intensity α-Fe/α-(Fe,Ni) peaks.

4.2 Microstructure Evolution

4.2.1 Morphology of initial powders used

Fig. 4.6 and Fig. 4.7 shows the morphology of initial raw powders of Fe and Ni at 250X, 500X, 2500X and 5000X magnifications, respectively. It is observed that the above metal powders are uniformly distributed. No severe agglomeration is observed in powder mi-crographs.

From Fig. 4.8, the morphology of $Fe_{70}Ni_{30}$ after ball milling can be observed. The uniformity and well distribution of particles can be seen for the powders after ball milling
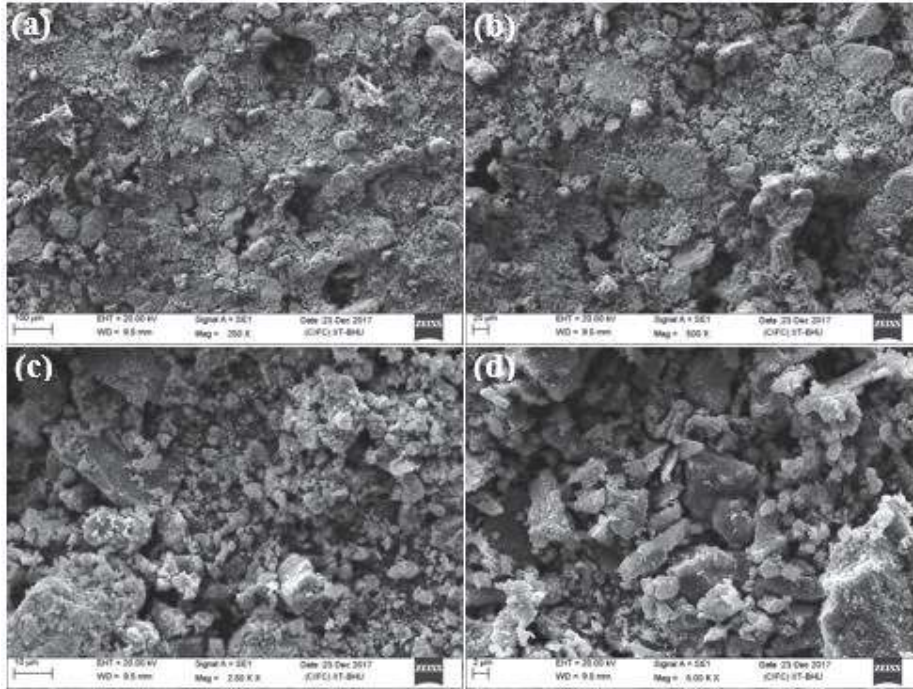
FIGURE 4.6: Powder morphology of raw Fe powder at (a) 250X, (b) 500X, (c) 2500X and (d) 5000X.
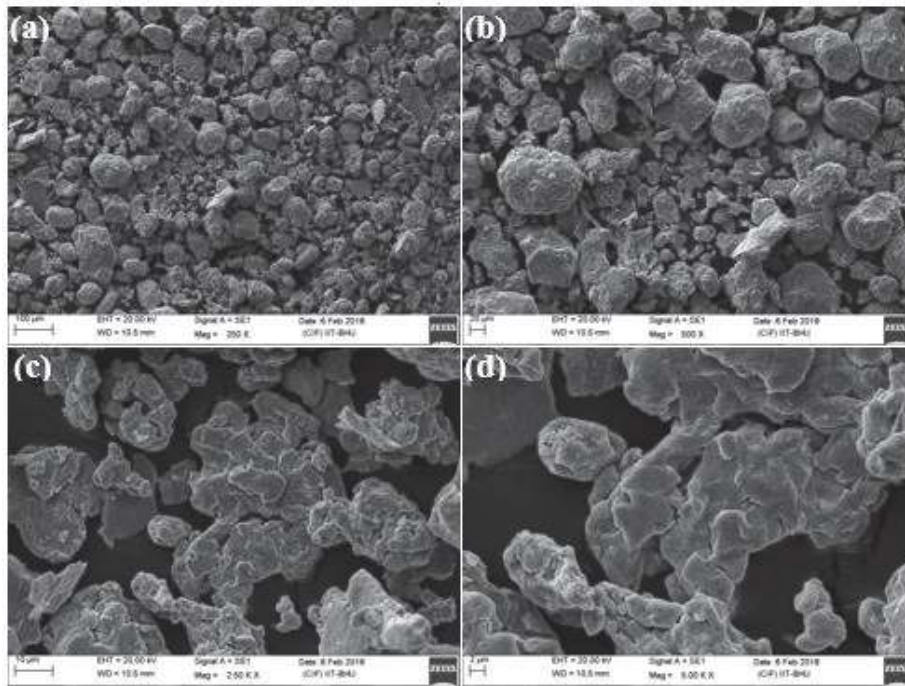

FIGURE 4.7: Powder morphology of raw Ni powder at (a) 250X, (b) 500X, (c) 2500X and (d) 5000X.
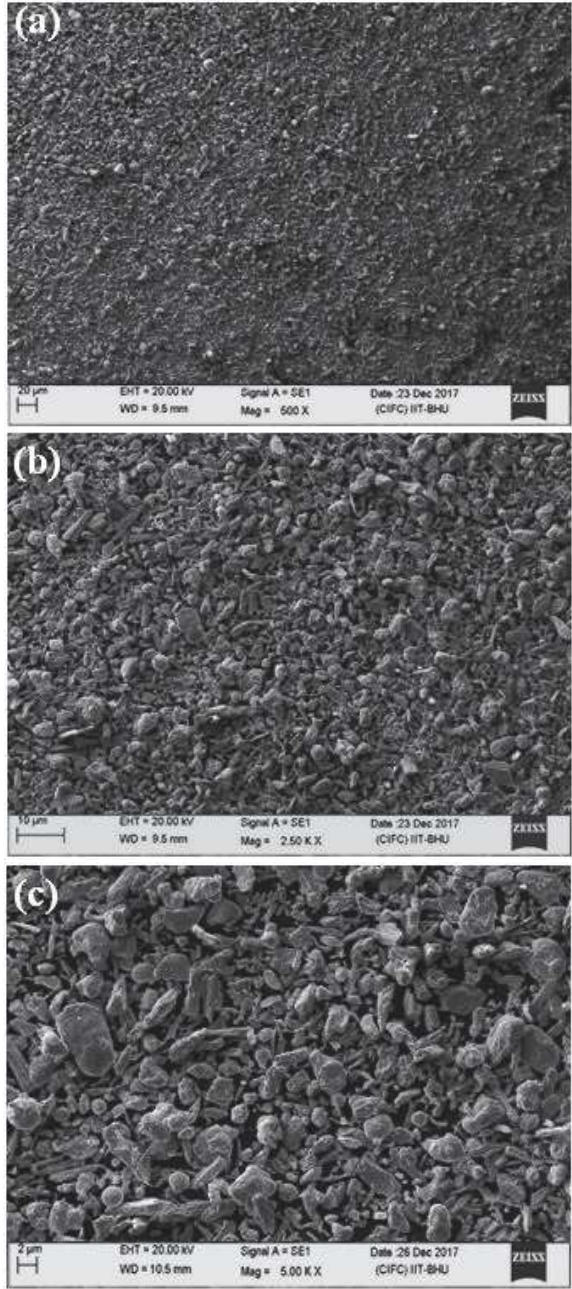
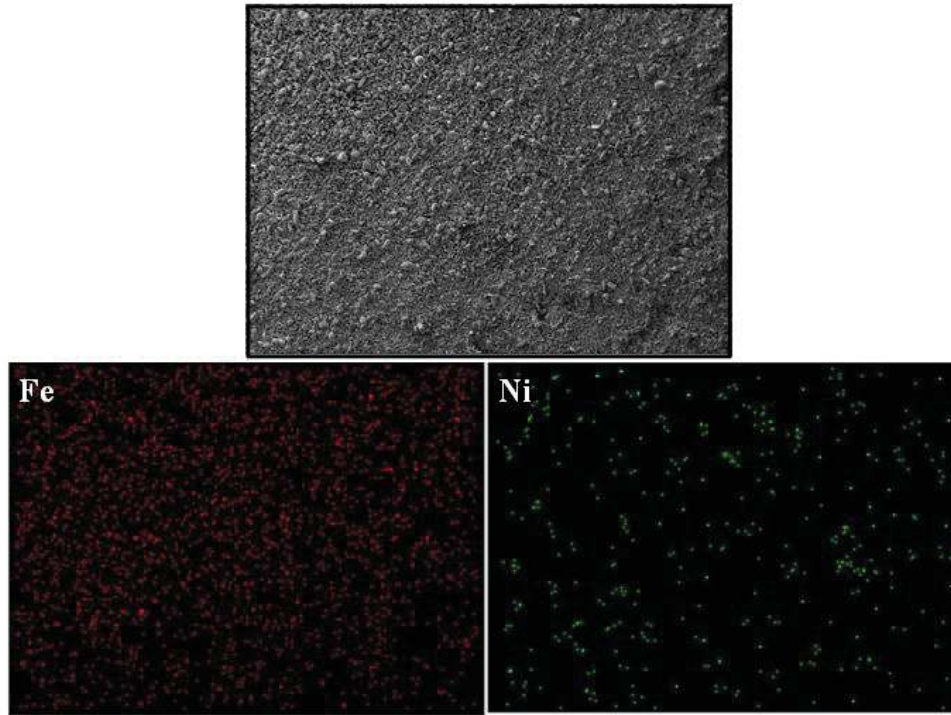FIGURE 4.8: Powder morphology of ball milled $Fe_{70}Ni_{30}$ powder at (a) 500X, (b) 2500X and (c) 5000X.

FIGURE 4.9: Elemental mapping of $Fe_{70}Ni_{30}$ ball milled powder.

which can be cleary evident in the electron mapping images as shown in Fig. 4.9. The elemetal analysis has shown the presence of 73 wt.% Fe and 27 wt.% Ni in the this region which is near to the selected composition of powder used for ball milling.

4.2.2 Microstructure of $Fe_{(100-x)}Ni_{(x)}$ sintered specimens

Fig. 4.10 shows the back scattered SEM images of the specimens sintered at 1000°C. It can be seen that two significant regions differing in contrast exist in the microstructure. The continuous dark region in micrograph may be identified as α-(Fe,Ni) and bright region may be identified as γ-(Fe,Ni). Both the regions can be distinguished with clear boundaries. There is an increase in the bright region, observed with increasing Ni content. This can also be correlated with the XRD results that γ-(Fe,Ni) formation increases

70

with increase in Ni percentage (Fig. 4.3 to Fig. 4.5).

Fig. 4.11 and Fig. 4.12 shows a similar change in microstructural behavior with composition variation for 1200 and 1250°C sintered specimens, respectively. The increase in the bright region is observed with increasing Ni concentration from 10 to 50 wt.%.

At lower Ni concentration, there is less Ni to diffuse into Fe. This leaves free Fe as unreacted form causing the differential stress and results in the pore formation if sintering is done at lower temperatures. Therefore, the presence of pores may be identified close to α phase, indicated as black spots. In the previous literature, compositional inhomogeneity in isolated grains in the microstructure is reported due to the low inter-diffusion coefficient of Fe and Ni at lower sintering temperatures [111].

It is interesting to note that the formation of γ-(Fe,Ni) is increased as the Ni content is increased from 10 to 50% at the same sintering temperature. Therefore, bright γ-(Fe,Ni) region is minimum as observed in $Fe_{90}Ni_{10}$ and maximum as observed in $Fe_{50}Ni_{50}$.

Fig. 4.13 shows a comparison of microstructures of specimens sintered at different temperatures. The change in microstructure with increasing the sintering temperature can be observed for each alloy composition. The difference is noted when sintering temperature is raised from 1000 to 1200°C as there is an increase in the bright region instead of clear phase boundaries at 1200°C. It can be concluded that more atoms get activated and diffuse for γ-(Fe,Ni) formation at 1200°C. Increasing the sintering temperature to 1250°C has again resulted in an increase in the bright region as compared to 1200°C sintered specimens which still supports the increased diffusion rate at higher sintering temperature. It has also resulted in the reduction of pore volume which has made the compositions denser.
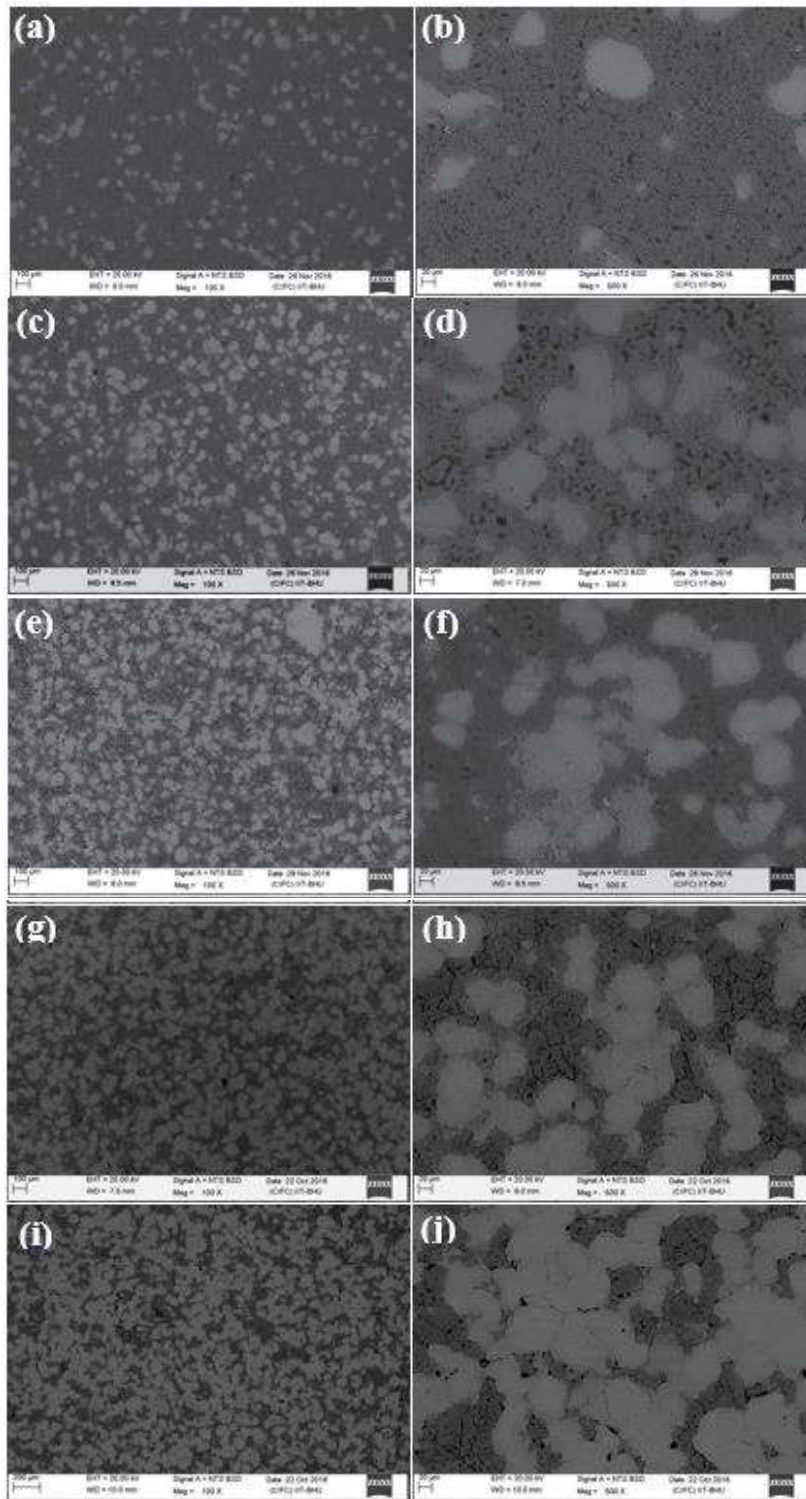
FIGURE 4.10: Back scattered SEM micrographs of 1000°C sintered specimens (a-b) $Fe_{90}Ni_{10}$, (c-d) $Fe_{80}Ni_{20}$, (e-f) $Fe_{70}Ni_{30}$, (g-h) $Fe_{60}Ni_{40}$, and (i-j) $Fe_{50}Ni_{50}$ at 100X and 500X magnifications.
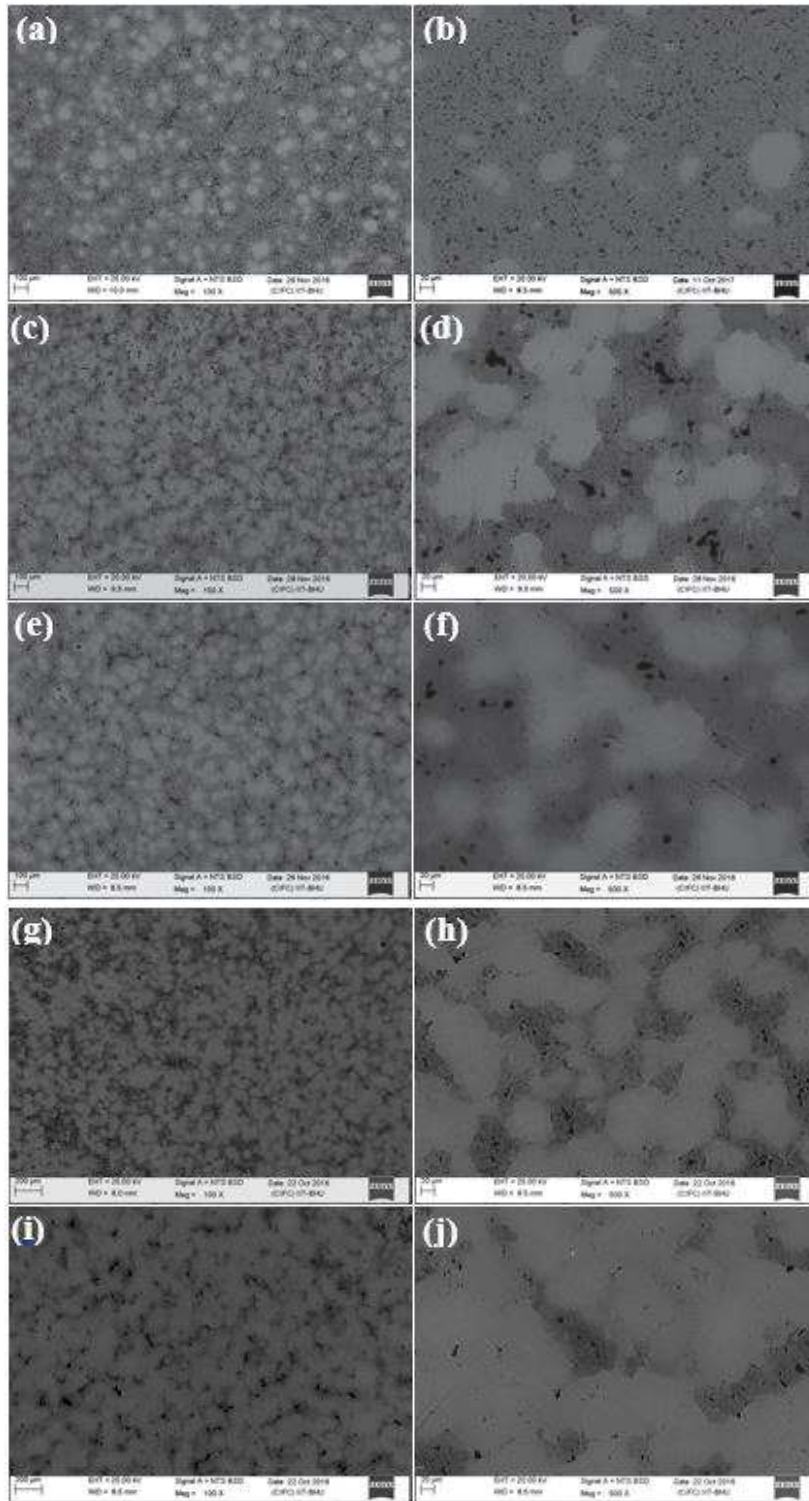
FIGURE 4.11: Back scattered SEM micrographs of 1200°C sintered specimens (a-b) $Fe_{90}Ni_{10}$, (c-d) $Fe_{80}Ni_{20}$, (e-f) $Fe_{70}Ni_{30}$, (g-h) $Fe_{60}Ni_{40}$, and (i-j) $Fe_{50}Ni_{50}$ at 100X and 500X magnifications.
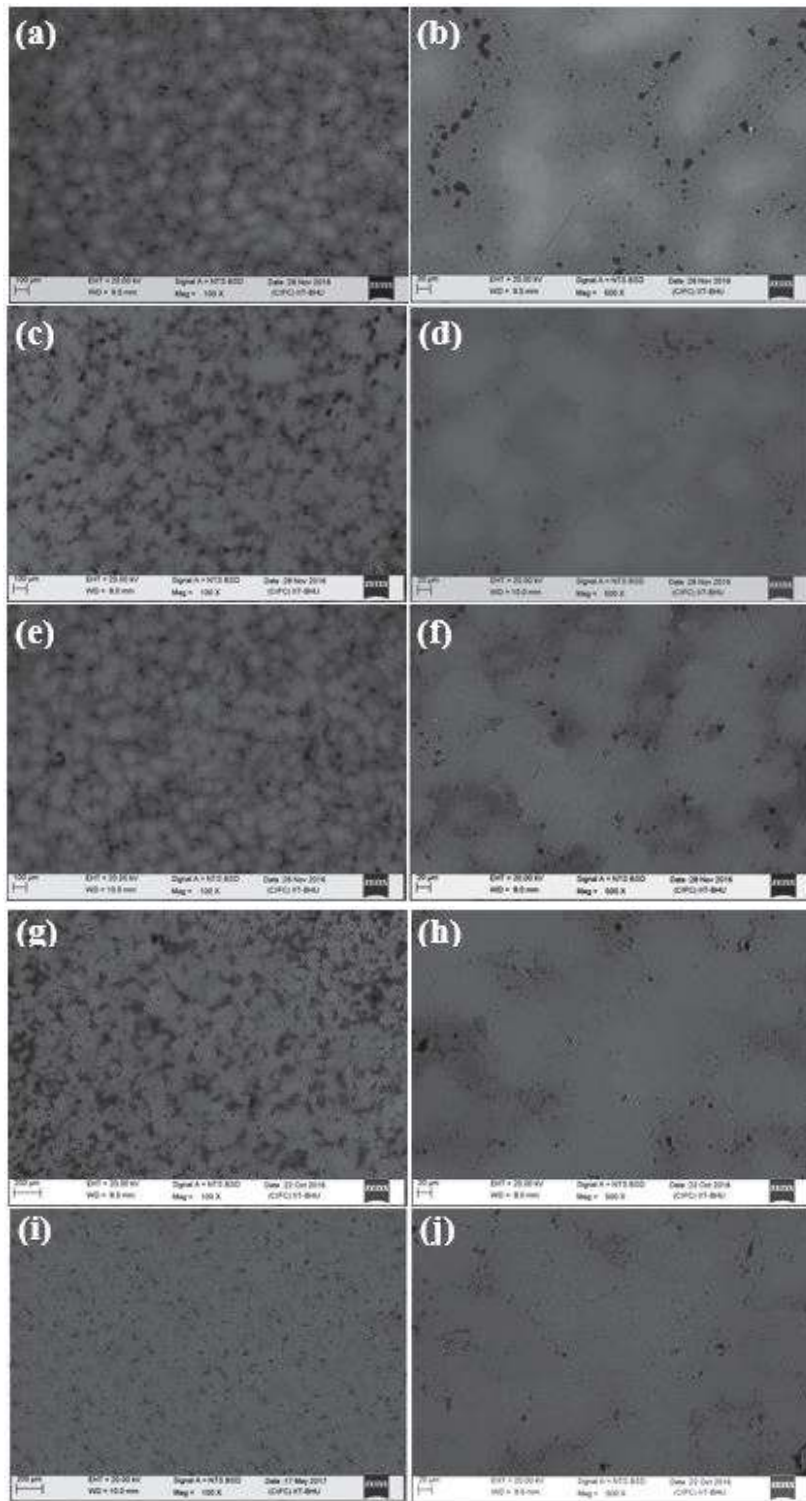
FIGURE 4.12: Back scattered SEM micrographs of 1250°C sintered specimens (a-b) $Fe_{90}Ni_{10}$, (c-d) $Fe_{80}Ni_{20}$, (e-f) $Fe_{70}Ni_{30}$, (g-h) $Fe_{60}Ni_{40}$, and (i-j) $Fe_{50}Ni_{50}$ at 100X and 500X magnifications.
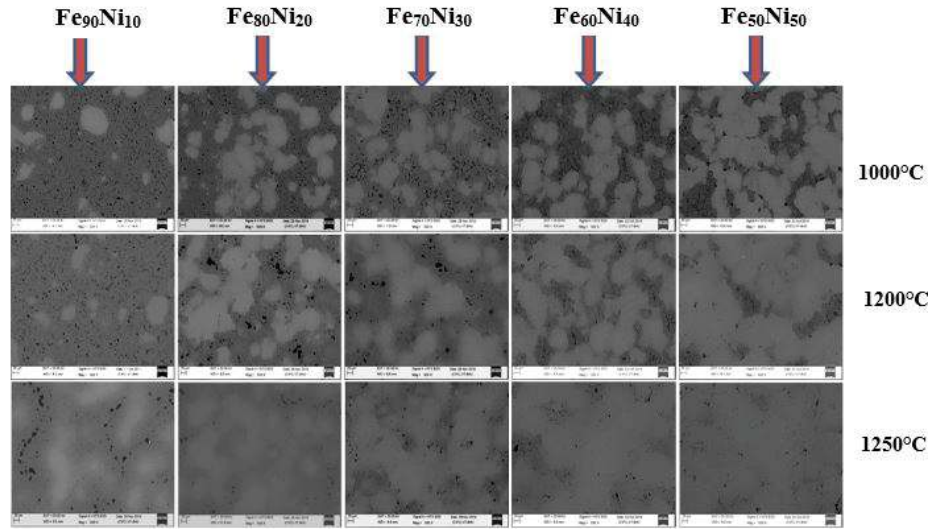
FIGURE 4.13: Comparative back scattered SEM micrographs of specimens sintered at different temperatures.

The inclusion of Ni reduces the phase transformation temperature of Fe-Ni alloys and enhances γ phase formation [112]. For $Fe_{50}Ni_{50}$, the microstructure is found to consist maximum bright region at 1250°C . The phase formation with increasing temperature and Ni content is in good agreement with XRD results. Fig. 4.14 shows the back scattered SEM images of chemically etched (a) $Fe_{90}Ni_{10}$, (b) $Fe_{70}Ni_{30}$ and (c) $Fe_{50}Ni_{50}$ specimens at 1000X magnification. The formation of phases with increasing Ni content can be identified with the help of this figure. Both the phases can be distinguished easily. Increasing the Ni content resulting in the bright phase region. In $Fe_{50}Ni_{50}$ specimen, dark region is small which can be seen near to the boundary. Fig. 4.15 shows the Comparative back scattered SEM micrographs of $Fe_{50}Ni_{50}$ specimens sintered at (a)1000°C, (b)1200°C and (c)1250°C at 1000X magnification after chemical etching. From this figure, the effect of sintering temperature on the phase formation of $Fe_{50}Ni_{50}$ can be observed. The grains of both the phases in different conrast can be distinguished easily at 1000°C but as the

75
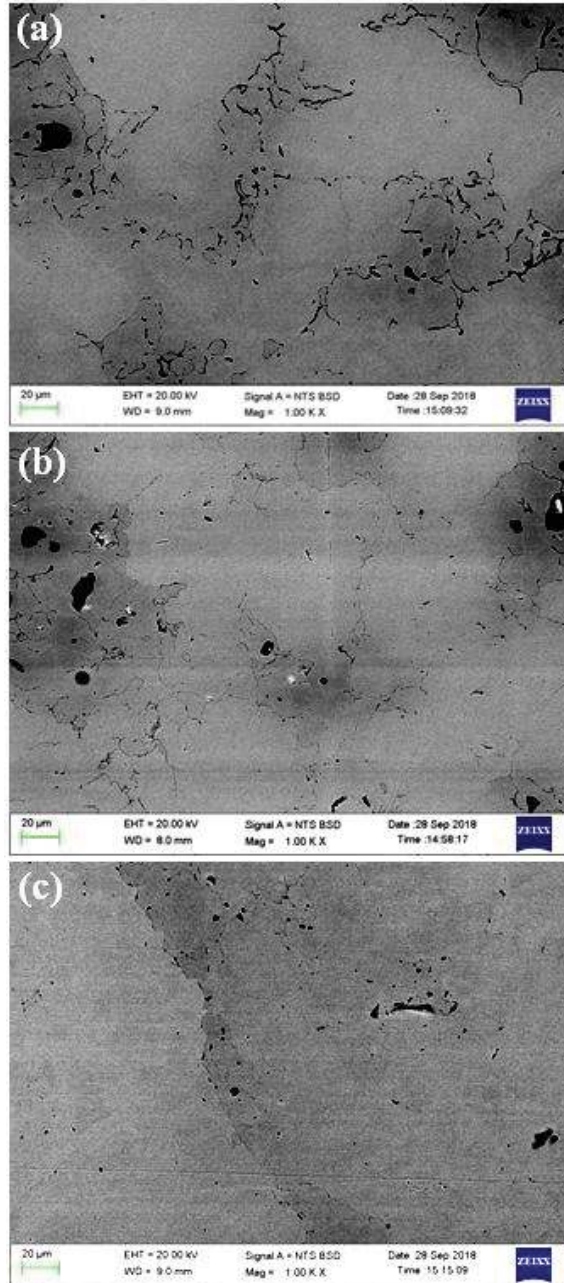
FIGURE 4.14: Comparative back scattered SEM micrographs of 1250°sintered and chemically etched (a) $Fe_{90}Ni_{10}$, (b) $Fe_{70}Ni_{30}$ and (c) $Fe_{50}Ni_{50}$ specimens at 1000X magnification.
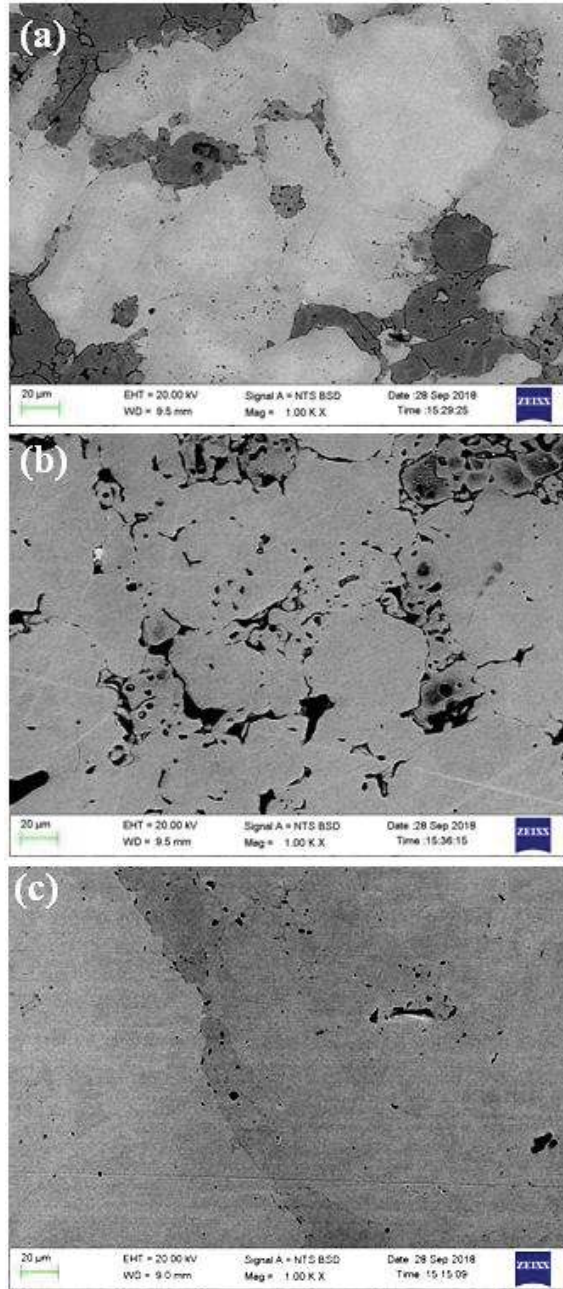
FIGURE 4.15: Comparative back scattered SEM micrographs of $Fe_{50}Ni_{50}$ specimens sintered at (a)1000°C, (b)1200°C and (c)1250°C at 1000X magnification after chemical etching.

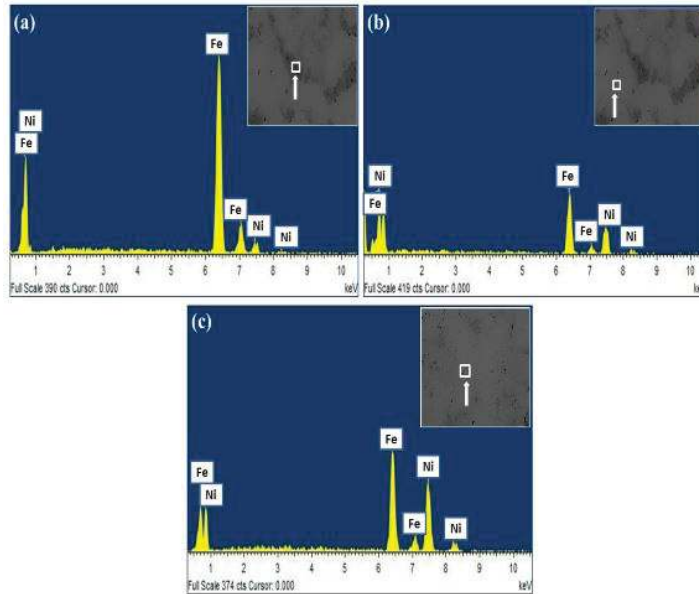FIGURE 4.16: EDX of $Fe_{50}Ni_{50}$ sintered at (a-b) 1200°C and (c) 1250°C.

sintering temperature is increased, the diffusion of Fe and Ni increased therefore a mi-crostructure with most bright region can be seen for specimen sintered at 1250°C. The dark phase region can only be seen near the boundary.

Fig. 4.16 (a-b) and Fig. 4.16 (c) show the EDX analysis of $Fe_{50}Ni_{50}$ sintered at 1200°C and 1250°C, respectively. Two different regions of 1200°C sintered specimens have been used for elemental analysis. The dark region (Fig. 4.16(a)) is found to contain around 93.05 atom% Fe and 6.95 atom% Ni. This is identified as α-(Fe,Ni) phase. In the bright region (Fig. 4.16 (b)), the observed Fe and Ni content is 30.21 atom% and 69.79 atom%, respectively. This region is confirmed as γ-(Fe,Ni) phase. The EDX of 1250°C (Fig. 4.16 (c)) sintered specimen is found to have bright region throughout the micrograph with Fe and Ni content as 58.48 and 41.52 atom%, respectively. This is again identified as γ-(Fe,Ni) phase.
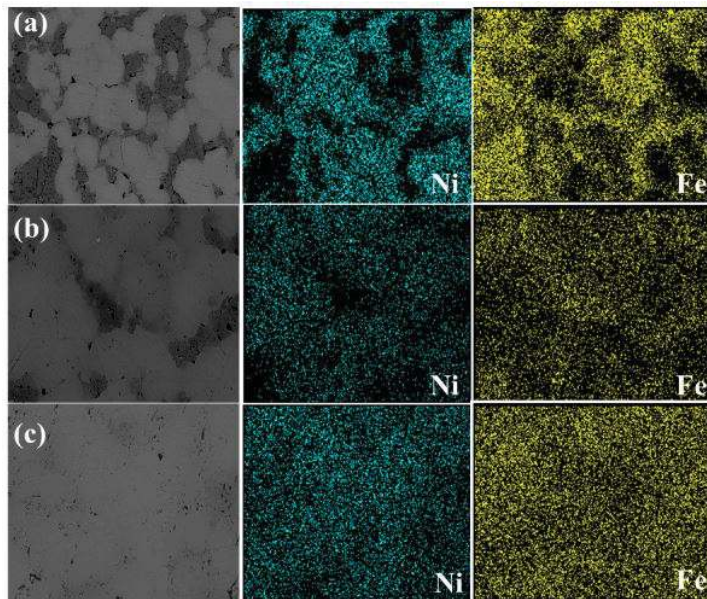
FIGURE 4.17: Elemental mapping of $Fe_{50}Ni_{50}$ sintered at (a)1000°C (b)1200°C and (c)1250°C.

Fig. 4.17 (a-c) shows the elemental mapping of $Fe_{50}Ni_{50}$ after sintering at (a) 1000°C (b) 1200°C and (c) 1250°C. The elements of both Fe and Ni have been captured and distinguished in figure. At 1000°C, the dark region is found to contain major Fe region whereas a very few Ni elements are present in this region, confirming the formation of α-(Fe,Ni) in the dark region. In the bright region, both Fe and Ni elements are present in significant proportion which can be taken as γ-(Fe,Ni) phase. It is observed from the figure that diffusion of Fe and Ni atoms has enhanced with increasing sintering temperature resulting in the change of Fe/Ni ratio. At 1250°C, both Fe and Ni atoms can be seen uniformly distributed for $Fe_{50}Ni_{50}$ in the micrograph. This results in the formation of γ-(Fe,Ni) throughout the micrograph. This is in agreement with the results obtained from XRD and microstructure analysis.

4.3 Density evolution

Fig. 4.18 shows the variation of density of $Fe_{(100-x)}Ni_{(x)}$ alloy specimens with sintering temperature and composition. It is observed that there is a decrease in density with increasing Ni wt. fraction. This behavior is observed for specimens sintered at all three sintering temperatures (i.e., 1000, 1200 and 1250°C). Chan et al. [110] have reported γ-(Fe,Ni) as a less dense phase and softer phase as compared to α-(Fe,Ni) which is also observed in our present study. An increase in γ-(Fe,Ni) is already discussed in the XRD and microstructure results in previous sections 4.1.2 and 4.2.2.

It has been reported earlier that addition of Ni reduces the abnormal grain growth and improves the densification behavior only up to 10 wt.%. Above this concentration, it shows a decrease in the density. This is attributed to the presence of differential stresses near the diffusion zone of Fe and Ni during the phase transformation of α-(Fe,Ni) to γ-(Fe,Ni) [54]. The enhancement in density with increasing sintering temperature is also observed from Fig. 4.18 which is in good agreement with the previous studies [113]. For Fe-Ni system, densification occurs due to inter-diffusion, if sintering is carried out at a temperature more than the transformation temperature of iron. In the present work, solid-state sintering leads to densification. This occurs in two stages. In the first stage, neck formation occurs between adjacent metal atoms by leaving the pores behind. The pore shrinkage and rounding occur in the second stage. The second stage dominates when the sintering is done at higher temperatures. This has been supported by the microstructure study in section 4.2.2. The presence of flaws plays the major role in altering the densification. Xue et al. [114] reported the formation of flaws due to the cluster formation of Fe
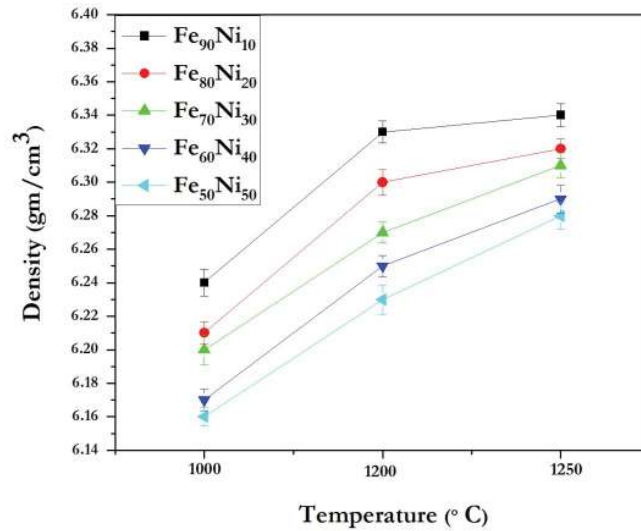
FIGURE 4.18: Temperature vs. Density plot of $Fe_{(100-x)}Ni_{(x)}$ alloy specimens sintered at different sintering temperatures.

rich region in Al-Fe system. Internal stresses are generated at the phase boundaries due to volume change. It can result in the nucleation of pores to relax these stresses. Presently, at a lower sintering temperature (i.e., 1000°C), there may be incomplete diffusion between Fe and Ni atoms which may result in unreacted clusters of iron-rich phase. This is responsible for the formation of pore channels. These iron-rich regions start getting consumed by Ni if the sintering is done at higher temperatures. Therefore, the presence of flaws (pores and pore channels) is expected to be reduced at higher temperatures. From the microstructure study (Fig. 4.10 to Fig. 4.12), the presence of pores is observed to be decreased with increasing sintering temperature for each composition aiding to enhanced densification.

4.4 Hardness

Fig. 4.19 shows hardness of $Fe_{(100-x)}Ni_{(x)}$ alloy specimens sintered at 1000, 1200 and 1250°C temperatures. It is observed that the hardness of $Fe_{(100-x)}Ni_{(x)}$ specimens decreases with increase in Ni content. From the phase and microstructure discussion (section 4.1.2 and 4.2.2), the variation in Ni concentration from 10 to 50 wt.% results in a significant increase in γ phase formation. Therefore the microstructure with more γ phase is found to have less hardness value which is in good agreement with the previous report where hardness was found to reduce with increasing Ni concentration in Fe-Ni system [113].
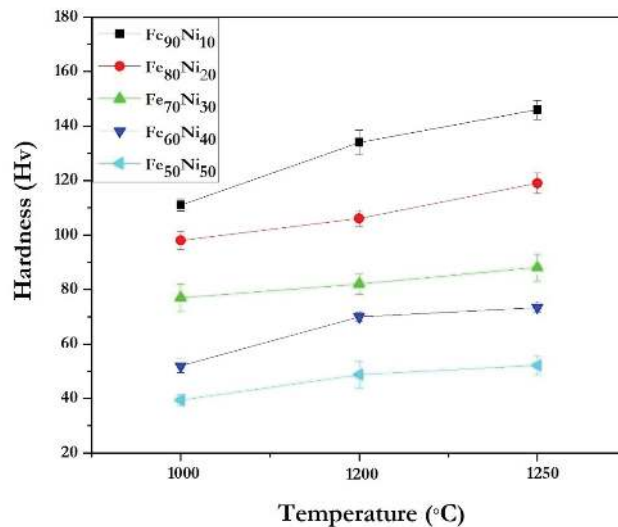

FIGURE 4.19: Temperature vs. Hardness plot of $Fe_{(100-x)}Ni_{(x)}$ alloy specimens sintered at different sintering temperatures.

Sintering temperature also plays an important role in altering the hardness of specimens. Along with the γ-(Fe,Ni) formation, flaw concentration also reduced significantly

with increasing sintering temperature. At lower sintering temperature, the defect concentration is higher which is clear from the microstructure analysis. When the indentation is done during hardness test, pores and micro cracks may combine and provide a path for the stress to get released which results in a decrease of hardness. Therefore, it is observed that the hardness value increases with increasing the sintering temperature for each composition. The increase in hardness at higher sintering temperature occurs as a result of solid solution hardening in case of alloy formation.

4.5   Dry sliding wear properties

Fig. 4.20 shows the coefficient of friction versus time plot for $Fe_{(100-x)}Ni_{(x)}$ sintered specimens at 20N applied load. It is observed that the COF value for sintered specimens varies with varying the composition. For $Fe_{90}Ni_{10}$ and $Fe_{80}Ni_{20}$, wear loss resulted due to the presence of brittle α-(Fe,Ni) as a major phase. These hard craters come out of the sample surface and move between the specimen surface and rotating disc which results in the wear loss of material.

An increase in γ-(Fe,Ni) formation resulted in less material loss, as the presence of soft γ phase provides support to the hard α phase thus reducing the material loss. A decrease in COF value is observed in $Fe_{70}Ni_{30}$ due to the considerable presence of both α and γ phases. For $Fe_{60}Ni_{40}$ specimen, comparative increase in soft γ-(Fe,Ni) phase resulted in an increase in the COF as high γ phase content results in more material removal from the specimen surface. These removed particles when coming between the specimen and disc surface results in high COF. Maximum wear loss and COF resulted in $Fe_{50}Ni_{50}$

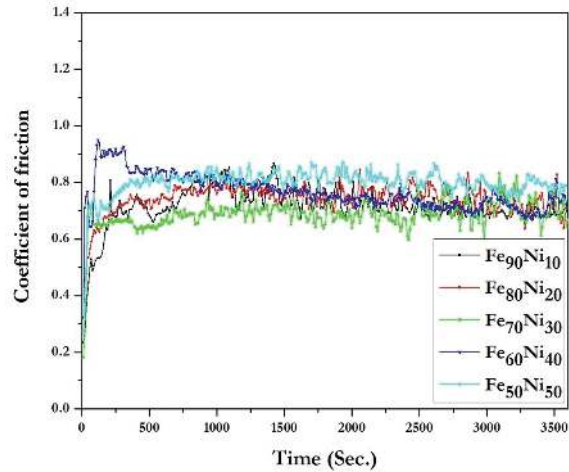FIGURE 4.20: COF vs. Time plot for specimens at 20N applied load.

specimen due to the maximum γ phase formation which is already discussed as a softer phase.

Fig. 4.21 (a-c) shows the wear rate of sintered specimens at different temperatures and loads. According to the Archard equation, $W = k(\frac{P}{H})$; wear depends on the hardness and ductility of a material [115, 116]. This is applicable for both adhesive and abrasive wear. Here W is wear rate, P is applied load, H is the hardness of the material and k is a constant which depends on the ductility of the material. In general, wear rate increases on increasing the applied load and thus the high wear rate is observed at higher normal load for each composition. Abrasive wear which is responsible for high wear loss occurs at higher applied load. Adhesive wear occurs at lower load and results in comparative low volume loss and delamination of the surface.

In the present work, compositions containing 10% and 20 wt.% Ni have α-(Fe,Ni) as a major phase. Generally, hardness is widely used for evaluating the wear resistance of
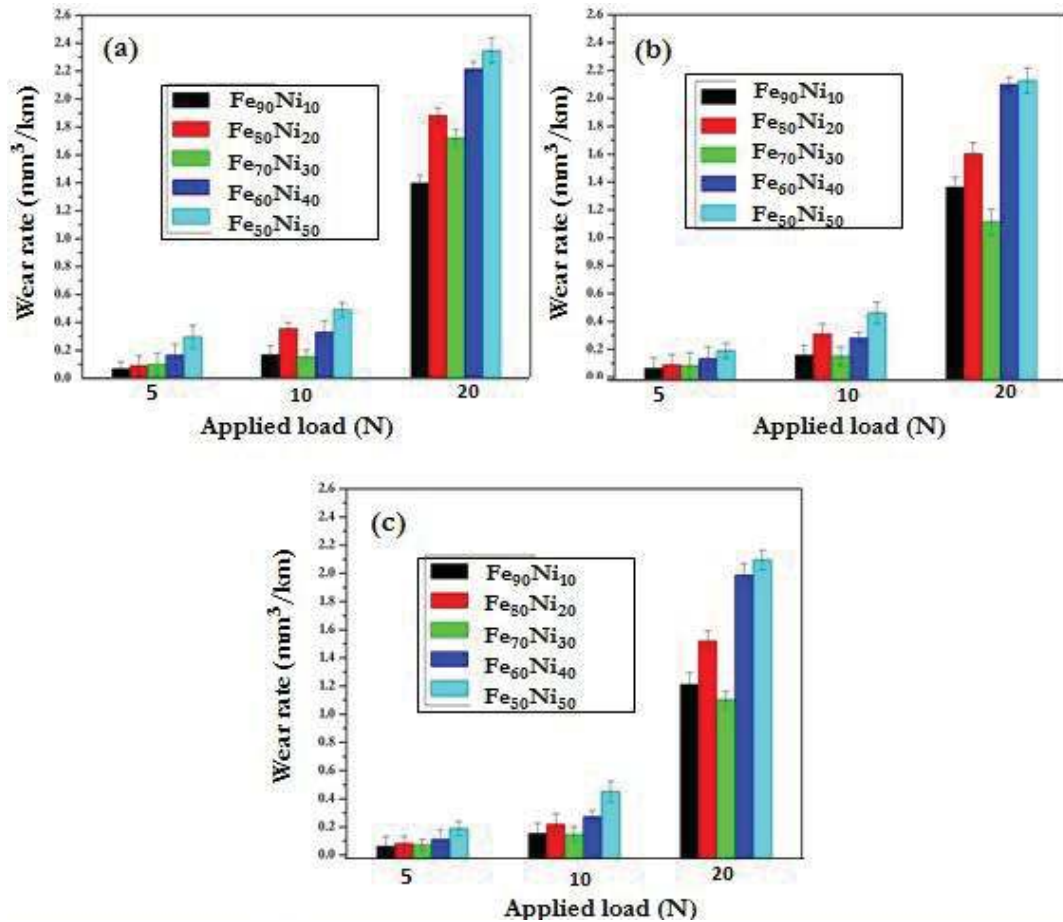
84

FIGURE 4.21: Wear rate of specimens sintered at (a) 1000, (b) 1200 and (c) 1250°C.

material, but it is not always a reliable approach. Wear resistance of material also depends upon the toughness of material which decreases with increase in hardness value [117].

Specimen with 30 wt.% Ni contains a significant amount of both α and γ-(Fe,Ni) phases. The hard α phase provides support and retards the plastic deformation of softer γ phase. This results in less volume loss as compared to $Fe_{80}Ni_{20}$ and $Fe_{90}Ni_{10}$ at each load. In $Fe_{60}Ni_{40}$ and $Fe_{50}Ni_{50}$ compositions, γ is present as a major phase which reduces the hardness of specimen. This increases wear rate due to more volume loss of softer γ phase.
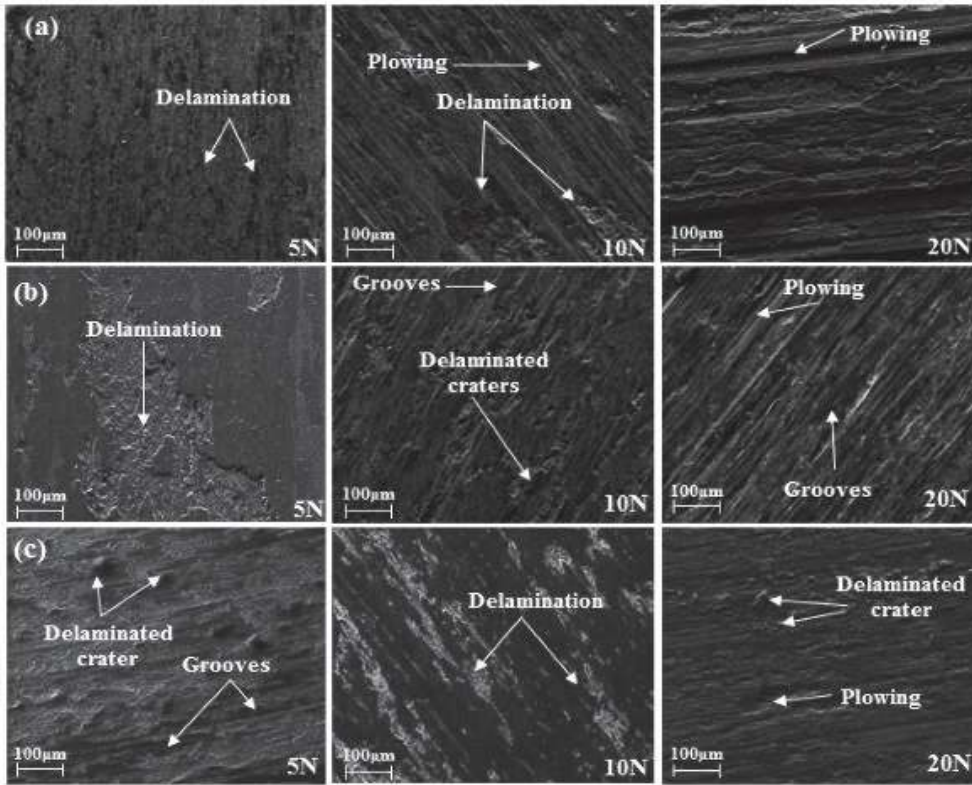
FIGURE 4.22: Worn surface SEM of $Fe_{90}Ni_{10}$ sintered at (a) 1000, (b) 1200 and (c) 1250°C.

Fig. 4.22 and Fig. 4.23 shows worn surface micrographs of sintered specimens examined under different loads. Under low load, delamination and slight grooves can be observed on the worn surfaces. At high load conditions, the presence of plowing mechanism is evident. Plowing is a process of material loss which occurs at the sideways of grooves and forms ridges. This plowing occurs during repeated sliding and results in hard asperities to come between the disc and specimen surface. This causes the damage of the specimen surface. In the present study, α-(Fe,Ni) asperities are removed from the surface and enhance the plowing mechanism. Fig. 4.22 shows the presence of deep grooves and delaminated craters along with plowing on the $Fe_{90}Ni_{10}$ worn surface micrograph under
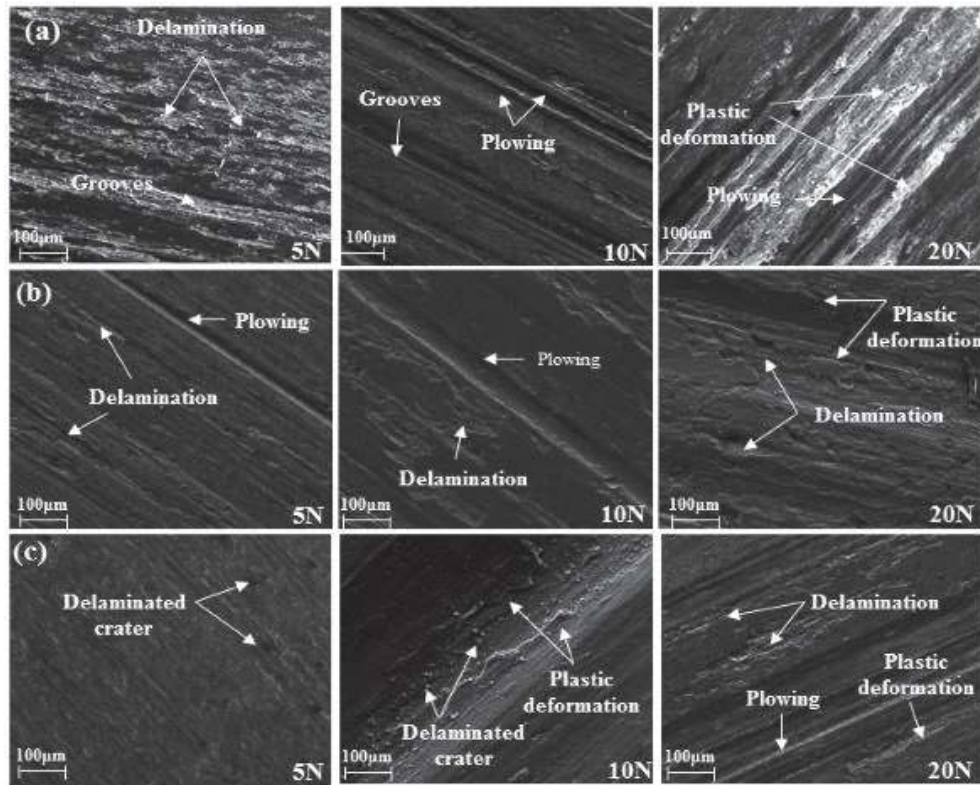
FIGURE 4.23: Worn surface SEM of $Fe_{50}Ni_{50}$ sintered at (a) 1000, (b) 1200 and (c) 1250°C.

high applied load.

Fig. 4.23 shows the worn surface micrographs of $Fe_{50}Ni_{50}$ specimen examined under different loads. Due to less hardness of $Fe_{50}Ni_{50}$ specimens, plastic deformation mechanism becomes dominating as a result of frictional heat during sliding under higher load (10 and 20N). Therefore delamination and plastic deformation are visible on the $Fe_{50}Ni_{50}$ worn surface due to more γ phase.

The presence of defects results in the loosely bound particles which may be readily removed during sliding. From the microstructure evolution (Section 4.2.2.), it is clear that on increasing the sintering temperature from 1000 to 1250°C decreases the defects

concentration. For specimens sintered at 1250°C, the reduction in defect concentration helps in retarding the particles removal during sliding. Therefore minimum wear rate is observed. The presence of fewer grooves and delaminated craters can be seen in the microstructure of specimens sintered at 1250°C. These are severe in case of samples sintered at 1000°C for each composition.

4.6 Scanning Kelvin Probe Force Microscopy (SKPFM)

Fig. 4.24 (a-f) shows the volta potential of specimen surfaces. Scanning Kelvin probe force microscope (SKPFM) technique was used to collect information about the surface potential of specimens. An atomic force microscope (AFM) NTMDT, NTEGRA Prima with silicon probe was used in semi contact mode. The results show the difference in the surface potential between different phases. Potential difference due to the presence of defects (pores and cracks) is also recorded using this technique. From the line scan, it is observed that the volta potential difference is positive at some places whereas it is negative at other sites.

In $Fe_{90}Ni_{10}$ specimen surface, two different contrast regions with different potential values were observed. As the Ni content is small in $Fe_{90}Ni_{10}$ specimen, therefore the γ formation is very less. Diffusion between Fe and Ni elements resulted in γ formation at local regions which can be seen as a dark region. This dark region shows anodic nature with a negative potential difference -4 to -8 mV. The remaining brighter region is cathodic with positive potential difference 6 to 11 mV. This brighter region is expected to be an iron rich phase (α-Fe-Ni) from the XRD analysis. In case of $Fe_{70}Ni_{30}$, a significant amount of
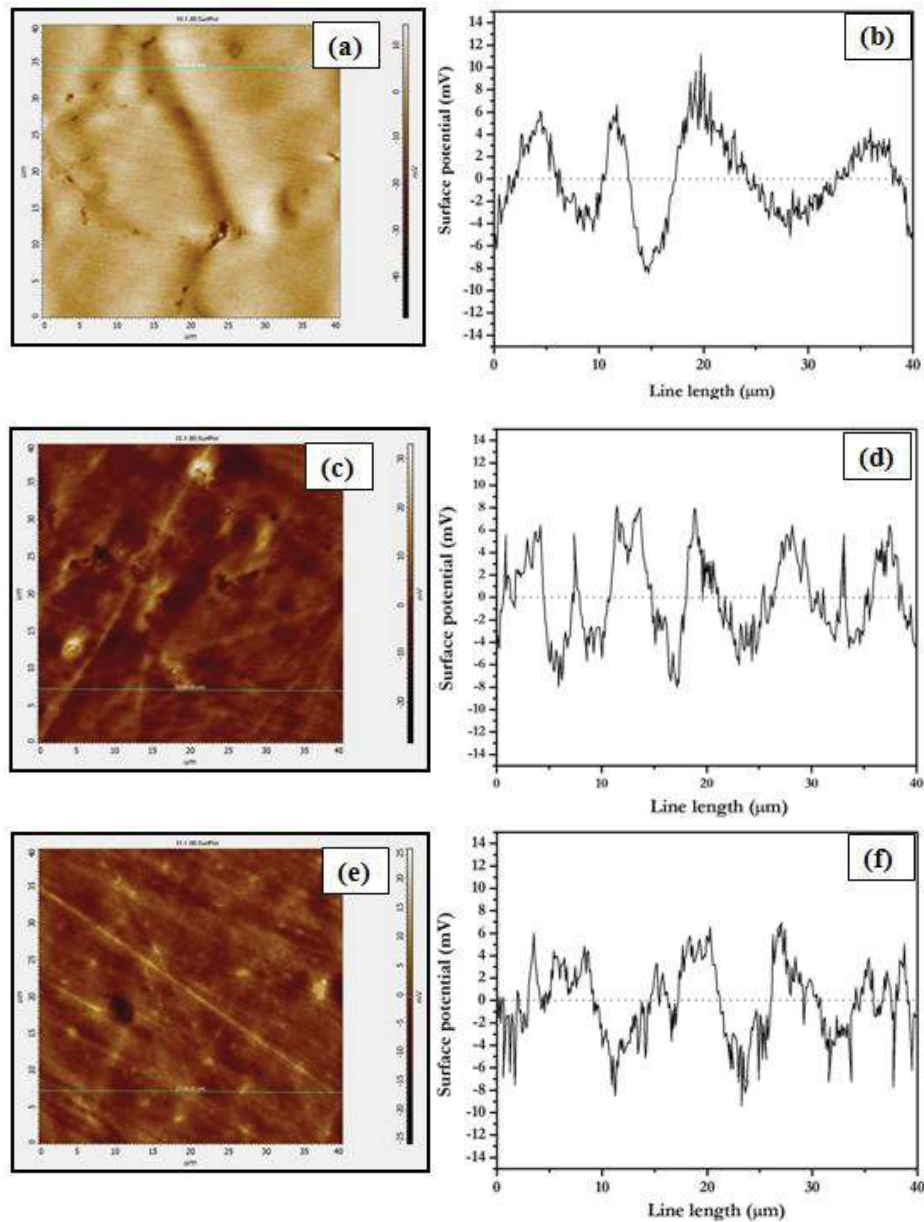
FIGURE 4.24: Surface potential of specimens (a-b) $Fe_{90}Ni_{10}$, (c-d) $Fe_{70}Ni_{30}$ and (e-f) $Fe_{50}Ni_{50}$.

γ evolved as a result of diffusion and both the phases α and γ are distributed throughout the exposed surface. The potential difference at the anodic region lies between -6 to -8 mV whereas, at the cathode region, this difference is 6 to 8 mV. In specimen $Fe_{70}Ni_{30}$

surface, the potential difference of surface is decreased as compared to $Fe_{90}Ni_{10}$. Also, the reduced potential difference between α (brighter region) and γ (as darker region) is observed. This is attributed to the increased γ formation in the specimen which causes more decrease in the potential difference between both the α and γ phases. The minimum potential value is observed in $Fe_{50}Ni_{50}$ due to the maximum γ formation. In $Fe_{50}Ni_{50}$, the potential difference at cathode region is 4 to 6 mV and -7 to -10 mV at anode region is which is less as compared to other specimens. It is already discussed that the maximum γ formation has resulted in $Fe_{50}Ni_{50}$ which is a softer phase as compared to α phase. The presence of scratches in $Fe_{50}Ni_{50}$ due to soft γ phase can also be seen on the polished surfaces. These scratches have also resulted in a slight increase of potential difference, but still, the potential difference is minimum as compared to other two specimens. It is expected that the decrease in potential difference between the cathode and anode region of the specimen surface will help in improving the corrosion resistance.

4.7   Electrochemical behavior

4.7.1   Potentiodynamic polarization Measurements

Fig. 4.25 shows the Tafel plot obtained during corrosion test. All the 1250°/1h sintered specimens were immersed in 3.5% NaCl solution (similar to sea water), and potentiodynamic polarization study is done to obtain Tafel plots. In the Tafel plots, extrapolation of cathodic and anodic potential regions resulted in different corrosion parameters, most importantly corrosion current. The obtained corrosion parameters are listed in Table. 4.1
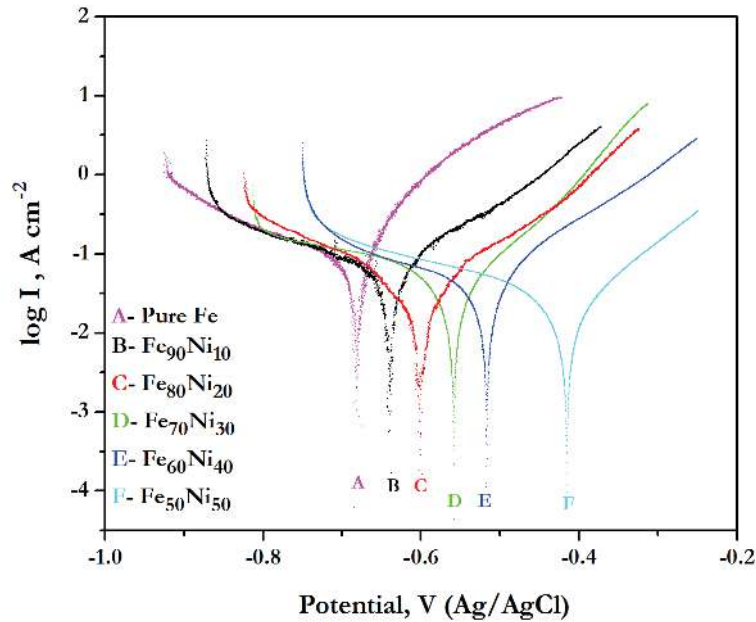
90

FIGURE 4.25: Tafel plots of $Fe_{(100-x)}Ni_{(x)}$ alloy specimens.

Pure iron is also immersed and tested in similar conditions for comparison with synthesized specimens. Corrosion current of $108.39\mu A/cm^2$ and corrosion potential of -739 mV is recorded for pure iron sample. For $Fe_{90}Ni_{10}$ specimen, 58.53 $\mu A/cm^2$ corrosion current and -638 mV corrosion potential is recorded. It is clear from results that corrosion current value has decreased and potential value has shifted to a positive direction for $Fe_{90}Ni_{10}$ as compared to pure iron specimen which shows the improvement in corrosion resistance with the addition of Ni. The reduction in corrosion current is again observed for $Fe_{80}Ni_{20}$, where the corrosion current is 50.20 $\mu A/cm^2$ and potential value is -591 mV. For $Fe_{70}Ni_{30}$, I_{corr} is 37.2 $\mu A/cm^2$ and E_{corr} is -549 mV and for $Fe_{60}Ni_{40}$, I_{corr} is 26.42 $\mu A/cm^2$ and E_{corr} is -518 mV which again shows the decrease in I_{corr} and shift of E_{corr} in the positive direction. Thus improvement in corrosion resistance occurs with increasing

91

TABLE 4.1: Electrochemical parameters obtained from potentiodynamic polarization curves.

S.No.	Specimen Name	$E_{corr}(mV)$	$I_{corr}(\mu A/cm^2)$	C_r(mpy)	$\mu_p\%$
1	Pure Fe	-739	108.3	118.12	-
2	$Fe_{90}Ni_{10}$	-638	58.5	69.20	41.5
3	$Fe_{80}Ni_{20}$	-591	50.2	59.79	50.0
4	$Fe_{70}Ni_{30}$	-549	37.2	41.59	65.2
5	$Fe_{60}Ni_{40}$	-518	26.4	33.44	72.0
6	$Fe_{50}Ni_{50}$	-425	22.1	28.36	76.2

Ni. The minimum I_{corr} is obtained for specimen $Fe_{50}Ni_{50}$ which is 22.11 $\mu A/cm^2$ whereas E_{corr} is -425 mV.The calculation of corrosion rate (C_r) and protection efficiency (μ_p) was done by using the obtained I_{corr} value [38] given below:
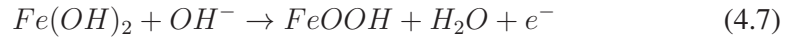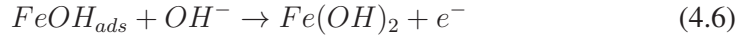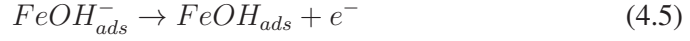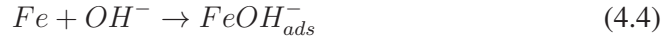
$$C_r(mpy) = \frac{0.13 I_{corr}(E.W.)}{d} \tag{4.1}$$

$$\mu_p\% = (\frac{I_{corr}^o - I_{corr}^i}{I_{corr}^o}) \times 100 \tag{4.2}$$

Where mpy is milli-inches per year, I_{corr} is corrosion current density ($\mu A /cm^2$), E.W. is equivalent weight (g), d is density (g/cm³), and I°corr and I^{i}corr are corrosion current densities of pure iron and alloy specimens respectively.

There is a decrease in corrosion current values with increase in Ni content of prepared alloys which indicates the decrease in the rate of anodic dissolution and hydrogen evolution reaction. The mechanism of corrosion reaction in $Fe_{(100-x)}Ni_{(x)}$ specimens in NaCl solution can be presented in two steps [118]:
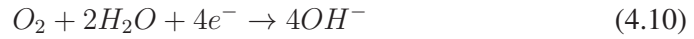
1. Anodic dissolution of Fe,

$$Fe \rightarrow Fe^{+2} + 2e^- \tag{4.3}$$

$$Fe + OH^- \rightarrow FeOH^-_{ads} \tag{4.4}$$

$$FeOH^-_{ads} \rightarrow FeOH_{ads} + e^- \tag{4.5}$$

$$FeOH_{ads} + OH^- \rightarrow Fe(OH)_2 + e^- \tag{4.6}$$

$$Fe(OH)_2 + OH^- \rightarrow FeOOH + H_2O + e^- \tag{4.7}$$

2. and/or

$$Fe + Cl^- \rightarrow FeCl_{ads} + e^- \tag{4.8}$$

$$FeCl_{ads} \rightarrow FeCl^+_{aq} + e^- \tag{4.9}$$

3. And the cathodic reaction is, reduction of molecular oxygen:

$$O_2 + 2H_2O + 4e^- \rightarrow 4OH^- \tag{4.10}$$

In case of pure iron, corrosion current value is very high as compared to other specimens. Consequently, Fe dissolution and hydrogen evolution process is fast which results in less corrosion resistance. In $Fe_{(100-x)}Ni_{(x)}$ specimens, increasing Ni from 10 to 50 wt.% resulted in the increased γ-(Fe,Ni) formation. From the previous literature, rust formation consisting of $Fe(OH)_2$ and $FeCl_2$ has been reported as a corrosion product. Therefore, the retardation of both the above equations is observed with the addition of Ni to form γ-(Fe,Ni) phase which is not easily attacked by Cl^- ions. In case of other alloy systems also, the addition of Ni has also been found responsible for alloy phase formation which has helped in reducing corrosion rate. EL-LATEEF et al. [119] have reported the formation

of γ-Zn$_3$Ni, responsible for corrosion protection of Zn-Ni alloy system. In the present work also, the reason behind the decrease of corrosion current value in Fe$_{(100-x)}$Ni$_{(x)}$ alloy system is the formation of γ-(Fe,Ni) phase with increasing Ni content. The grains of this phase may have higher hydrogen over potential than that of pure Fe and therefore decrease the density of active sites in alloy.

4.7.2 Electrochemical Impedance Spectroscopy (EIS)

The study of impedance measurement and its comparison is a very useful technique to understand the corrosion behavior of any system. The detailed information of the corrosion process at the electrode-electrolyte interface can be obtained by interpretation of the EIS data with an appropriate equivalent circuit (EC). The Nyquist plots obtained using EIS technique for pure iron and differently prepared alloy samples are shown in Fig. 4.26. The impedance spectra of pure Fe consists a single capacitive semicircle showing that the
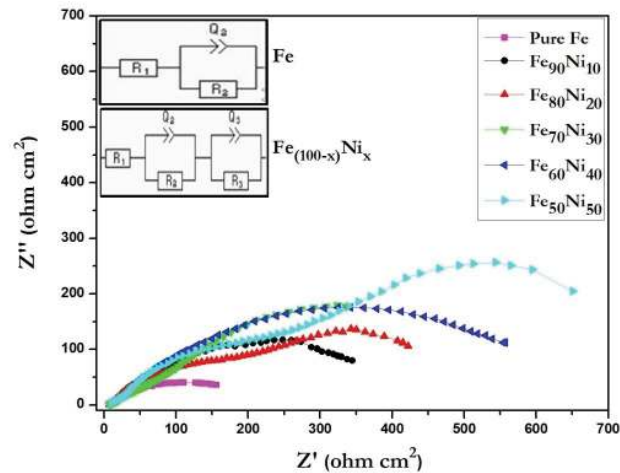

FIGURE 4.26: Nyquist plots for Fe$_{(100-x)}$Ni$_{(x)}$ alloy specimens.

94

corrosion process was mainly charge transfer controlled [120]. It is seen that the diameter of the semicircle for the alloy system is quite large than that of pure Fe suggesting that the $Fe_{(100-x)}Ni_{(x)}$ alloy is more corrosion resistant than pure Fe. The EIS data has been fitted to appropriate equivalent circuits to properly interpret the results. The EC for pure Fe and $Fe_{(100-x)}Ni_{(x)}$ samples are shown as inset in Fig. 4.26. The EC fitted of pure Fe sample contains one pure resistive part (R_1) that represents the resistance between working and reference electrode. This is in series with Q, the constant phase element (CPE) which represents the capacitance in parallel with a resistance (R_2). This is for the charge transfer process of the electrode in the electrolyte system. The EC fitted for $Fe_{(100-x)}Ni_{(x)}$ samples contains one additional CR circuit which is in series with the circuit shown for pure Fe. The additional capacitance and resistance for the alloy system may be due to the presence of another phase in the specimens. XRD results show that the $Fe_{(100-x)}Ni_{(x)}$ samples consist of two phases and thereby the electrolyte faces two types of grains at the electrode surface.

4.7.3 Microstructure study after corrosion

Fig. 4.27 shows the SEM images of specimen surfaces after corrosion test. The pure iron surface is observed as the most affected due to corrosion whereas $Fe_{50}Ni_{50}$ surface is least affected among all the compositions. In alloy specimens, it is found that the iron-rich phases α-(Fe,Ni) have more active sites for corrosion as compared to γ-(Fe,Ni) in the presence of the salt medium.
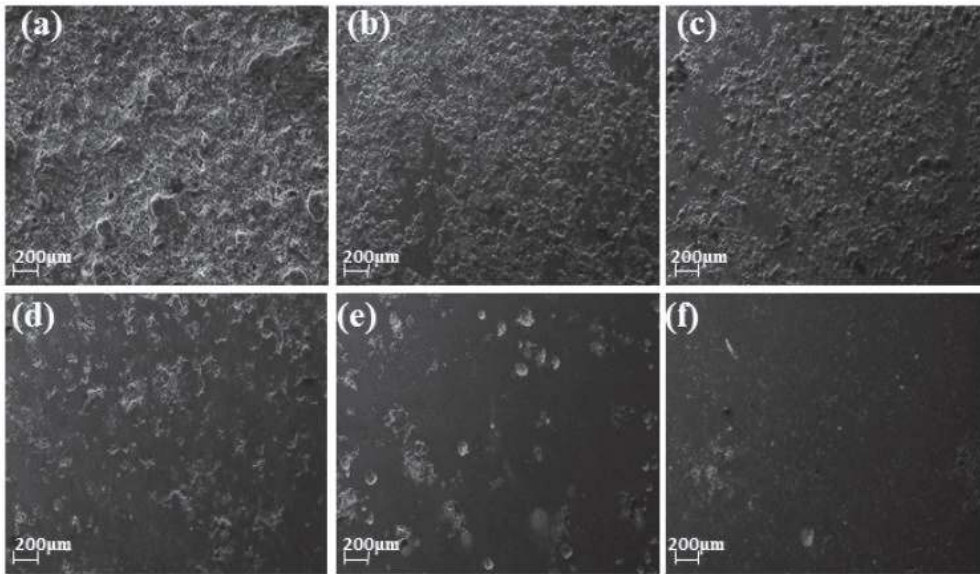
FIGURE 4.27: SEM micrographs of (a) Pure Fe, (b) $Fe_{90}Ni_{10}$, (c) $Fe_{80}Ni_{20}$, (d) $Fe_{70}Ni_{30}$, (e) $Fe_{60}Ni_{40}$, and (f) $Fe_{50}Ni_{50}$ specimen surfaces after corrosion test.
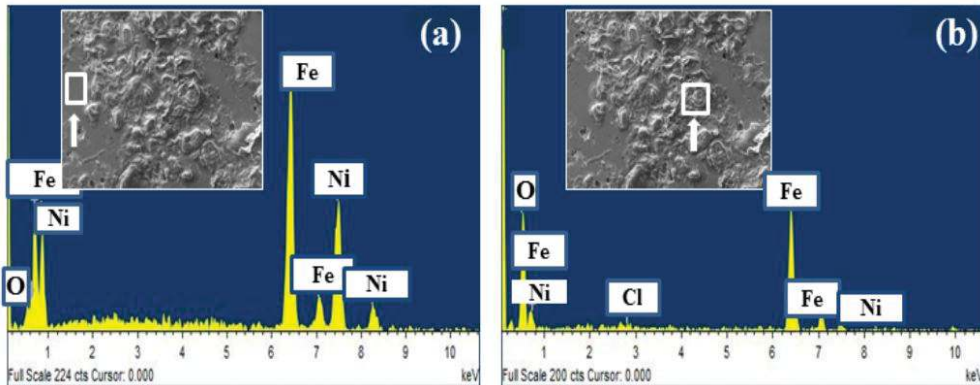

FIGURE 4.28: EDX of the corroded surface at different regions.

It is confirmed by the impedance spectroscopy and Tafel polarization that the samples containing more γ phase show more corrosion resistance in the salted medium. Therefore the effect of electrolyte on the $Fe_{50}Ni_{50}$ specimen surface was least due to the maximum γ phase formation. From Fig. 4.28 (a-b), EDX of the corroded surface have been recorded. Two different regions have been selected for the elemental analysis. The region which is not affected by the electrolyte (Fig. 4.28 (a)) is found to contain Fe and Ni elements in

a significant proportion which is expected to be γ phase. The elemental analysis of the second region (Fig. 4.28 (b)) shows the presence of Cl^-, oxygen and abundant Fe content which is expected as iron-rich phase α-(Fe,Ni). Therefore, it is suggested that the region which has more γ phase in the microstructure is less affected by corrosion. Presence of Cl^- and oxygen supports the formation of ferric chloride and hydroxide in the rust layer.

4.8   Summary of the chapter

In the current chapter, different $Fe_{(100-x)}Ni_{(x)}$ alloy specimens were synthesized by P/M route and sintered at different temperatures. The important points observed from this chapter are as follows:

1. XRD results have shown the γ-(Fe,Ni) formation with increasing Ni concentration.

2. Along with the Ni concentration, sintering temperature has exhibited an important role in phase formation. γ phase was found to be increased with increasing sintering temperature from 1000 to 1250°C.

3. Similar behavior was also observed from the microstructure analysis. The bright phase representing γ-(Fe,Ni) has increased with increasing Ni content and sintering temperature.

4. Maximum γ- formation was achieved in $Fe_{50}Ni_{50}$ specimen after sintering at 1250°C/1h due to higher Ni content and sintering temperature.

5. Ni content and sintering temperature have also affected the densification of alloy specimens. As, it was found that the γ-(Fe,Ni) phase is a soft and less dense phase as compared to α-(Fe,Ni) therefore increasing the Ni content resulted in less densification. Increasing the sintering temperature has also reduced the defect concentration resulting from diffusion and grain growth. Therefore, the increase in densification was observed with increasing the sintering temperature.

6. Presence of significant amount of both γ-(Fe,Ni) and α-(Fe,Ni) has resulted in the increase in wear resistance for $Fe_{70}Ni_{30}$. Wear resistance has been found to be decreased in the compositions $Fe_{90}Ni_{10}$ and $Fe_{50}Ni_{50}$ due to presence of high α-(Fe,Ni) and γ-(Fe,Ni) phases, respectively.

7. Samples containing more γ phase were found to be more resistant to corrosion in saline medium (3.5% NaCl aqueous solution). Potentiodynamic polarization measurements have shown a decrease in corrosion current for the samples containing more γ phase. This has been supported by the increased diameter of the semicircle in impedance spectroscopy which represents the more corrosion resistance in samples containing more γ phase. Maximum corrosion protection efficiency was achieved in $Fe_{50}Ni_{50}$ samples due to maximum γ phase presence.